Physics of Fluids

Structural dynamics of water in a supersonic shockwave

Cite as: Phys. Fluids **35**, 016126 (2023); https://doi.org/10.1063/5.0131457
Submitted: 20 October 2022 • Accepted: 07 January 2023 • Accepted Manuscript Online: 07 January 2023 • Published Online: 27 January 2023

Malte Vassholz, Hannes P. Hoeppe, Johannes Hagemann, et al.

Physics of Fluids ARTICLE scitation.org/journal/phf

Structural dynamics of water in a supersonic shockwave

Cite as: Phys. Fluids **35**, 016126 (2023); doi: 10.1063/5.0131457
Submitted: 20 October 2022 · Accepted: 7 January 2023 ·
Published Online: 27 January 2023

Malte Vassholz,[1] Hannes P. Hoeppe,[1] Johannes Hagemann,[2,3] Juan M. Rosselló,[4,5] Markus Osterhoff,[1] Robert Mettin,[5] Johannes Möller,[6] Markus Scholz,[6] Ulrike Boesenberg,[6] Jörg Hallmann,[6] Chan Kim,[6] Alexey Zozulya,[6] Wei Lu,[6] Roman Shayduk,[6] Anders Madsen,[6] and Tim Salditt[1,a)]

AFFILIATIONS

[1]Institut für Röntgenphysik, Georg-August-Universität Göttingen, D-37077 Göttingen, Germany
[2]CXNS—Center for X-ray and Nano Science, Deutsches Elektronen-Synchrotron DESY, D-22607 Hamburg, Germany
[3]Helmholtz Imaging Platform, Deutsches Elektronen-Synchrotron DESY, D-22607 Hamburg, Germany
[4]Faculty of Mechanical Engineering, University of Ljubljana, SVN-1000 Ljubljana, Slovenia
[5]Drittes Physikalisches Institut, Georg-August-Universität Göttingen, D-37077 Göttingen, Germany
[6]European X-Ray Free-Electron Laser Facility, D-22869 Schenefeld, Germany

Note: This paper is part of the special topic, Cavitation.
[a)]**Author to whom correspondence should be addressed:** tsaldit@gwdg.de

ABSTRACT

We explore the pressure evolution and structural dynamics of transient phase transitions in a microfluidic water jet after laser-induced dielectric breakdown. To this end, we use a combined approach of near-field holography with single femtosecond x-ray free-electron laser pulses and x-ray diffraction. During cavitation and jet breakup, we observe shock wave emission along the jet. The formation of the shock-wave is accompanied by pronounced changes in the structure factor of water as an evidence by a shift in the water diffraction peak. This indicates a transition to a high density liquid structure induced by the transient pressure increase.

I. INTRODUCTION

The exceptional properties of water are believed to be deeply rooted in the molecular structure of this most important fluid on earth. Molecular interactions, short range order, and the hydrogen bond network have all received abiding interest in view of their role for thermodynamic response functions and the equilibrium phase diagram. This research has required structural analysis of water in the liquid and also the supercooled, amorphous state, as reviewed in Refs. 1–4. From x-ray and neutron diffraction in the supercooled regime, it was since long known that amorphous ice can be presented in two forms with different densities, namely, high-density[5] and low-density amorphous ice.[6] Later it was realized that not only amorphous ice but also liquid water can exist in two different molecular configurations with higher and lower densities, respectively.[7] In its low-density liquid (LDL) form, water molecules tend to arrange in a tetrahedral structure, whereas for the high-density liquid (HDL) observable at high pressures, the second coordination shell of water molecules seems to collapse.[8] This duality of a water structure may possibly also play a role already at ambient conditions.[9]

The advent of high brilliance x-ray radiation, both at synchrotron radiation sources and x-ray free-electron lasers (XFELs), has more recently spurred investigations of water, mainly in the low temperature, undercooled regime,[10–13] but also under ambient conditions, and at high temperatures/high pressures.[14–17] Evidence for a liquid–liquid transition (LLT) between HDL and LDL was reported in the synchrotron study of Ref. 11 and more recently confirmed with XFEL pulses.[12] Beyond equilibrium conditions, strongly driven processes are of interest, in particular, in view of the extreme pressures, which can be reached by dynamic (transient) compression.[18,19] For isentropic compression of water, a crystallization to body-centered cubic ice (ice VII) was observed within less than 10 ns via heterogeneous nucleation.[20] The heating effects during shock compression and, more generally, the compression path can be varied by the experimental geometry and parameters. However, this also entails a spatial variation, since the

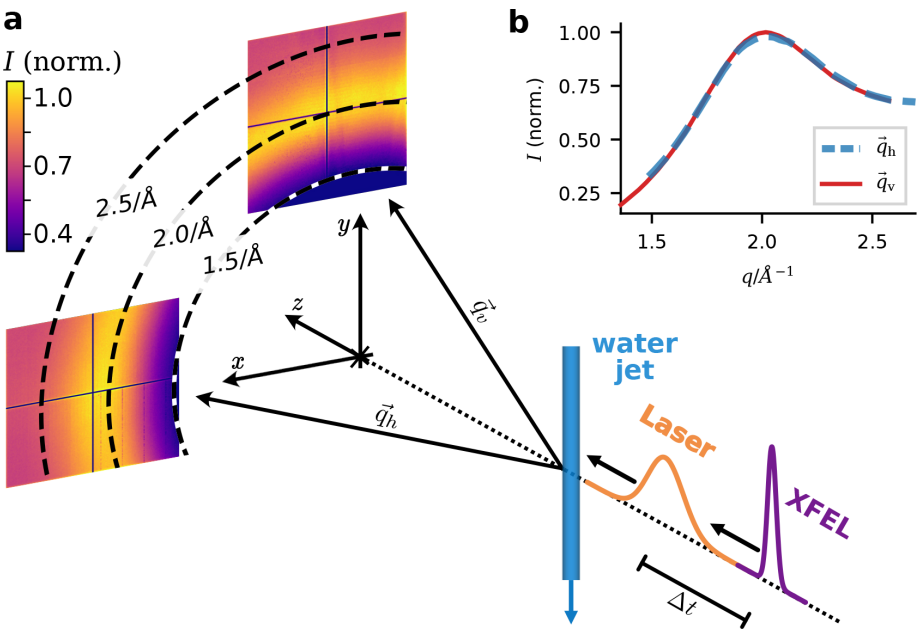

FIG. 1. Diffraction from a water jet—the experimental setup. (a) A μ-fluidic water jet is excited by a focused nanosecond laser pulse and probed after time delay Δt by the XFEL pulse. For x-ray diffraction (WAXS configuration), the foci of the pump laser and XFEL beam are aligned to the same spot in the water jet, while the jet and laser focus are moved downstream from the x-ray focus for imaging of plasmas and cavitation bubbles (NFH configuration). The diffraction signals in vertical ($\vec{q}_v$) and horizontal ($\vec{q}_h$) directions are acquired on two pixel array detectors. (b) Normalized, azimuthally averaged intensity $I(q)$ of the signal for both detectors as shown in (a).

excitation conditions vary strongly, for example, with the distance to the laser focus. Hence, diffraction studies require not only temporal synchronization but also a spatial confinement. To spatially control the location where the structural dynamics of water is probed in an inhomogeneous and transient perturbation such as a shockwave and to provide complementary density information, we here combine the pump-probe diffraction in the wide-angle x-ray scattering (WAXS) regime with our recently developed x-ray near-field holography (NFH) scheme.[21,22] By using advanced phase retrieval and a generalized empty-beam division,[21] we showed earlier that the local densities inferred from phase retrieval can reveal the pressure profile of a shockwave[22] in the regime of several GPa. We now use this NFH scheme in combination with WAXS to investigate the structural dynamics of water following dielectric breakdown induced by an infrared (IR) laser pulse and during the subsequent formation and growth of a cavitation bubble. For successive sample replenishment, and in particular, to circumvent the otherwise dominating signals of unperturbed water, we use a laminar microfluidic water jet. The main goal of the work is to evidence a transient transformation of the molecular water structure within the shockwave. By combining diffraction with imaging, we can precisely place the diffraction probe in space and time with respect to the expanding cavitation bubble in the jet. We can, hence, cover length scales from the molecular level to the mesoscale, where the pronounced non-equilibrium hydrodynamic effects manifest themselves, while being intrinsically coupled to the molecular water structure. Importantly, not only the combination of the technique but also the WAXS experiment on a shocked water alone is a novelty. The experimental schemes for the two modalities are sketched in Figs. 1 and 2.

II. EXPERIMENT

A. Experimental approach and schemes

The experiments were performed at the Materials Imaging and Dynamics (MID) instrument[23] of the European X-ray Free-Electron Laser.[24,25] Focused nanosecond infrared (IR) laser pulses were used to induce dielectric breakdown in a μ-fluidic water jet (Fig. 1). A pump-probe scheme with variable time delay Δt (Ref. 26) was implemented

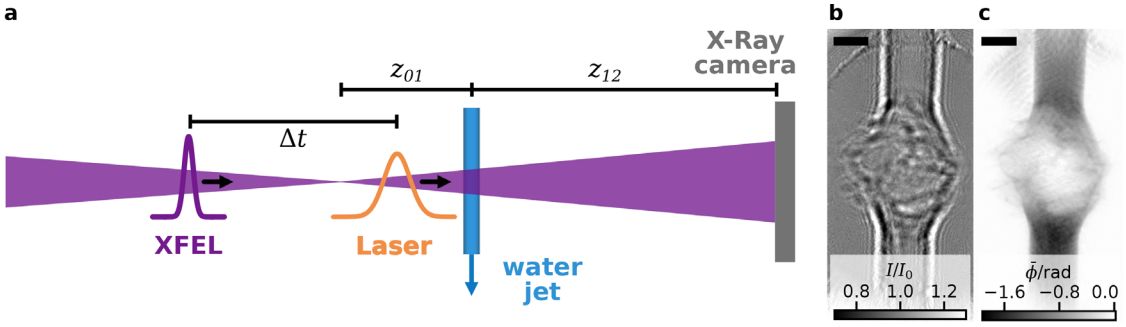

FIG. 2. Near-field holography. (a) The water jet is illuminated by the diverging x-ray beam. The x-ray holograms are acquired with a scintillation-based camera. (b) Empty-beam corrected x-ray hologram of the perturbed water jet with $\Delta t = 9$ ns. (c) Phase shift $\bar{\phi}$ of (b) after iterative phase retrieval. Scale bar: 20 μm in (b) and (c).

to record both WAXS and NFH signals. In both configurations, WAXS as well as NFH, the IR laser was focused into the water jet. With 6 ns pulse duration and 17 mJ pulse energy, the IR laser delivered peak intensities of about $\lesssim 3 \times 10^{10}$ W cm^{-2}. The XFEL was operated in a single-bunch mode with 10 Hz repetition rate at 17.8 keV photon energy, 660 μJ average energy per pulse, and a pulse duration of less than 100 fs.[25,27] A stack of aberration-corrected, nano-focus compound refractive lenses (CRLs)[28–30] was used to focus the XFEL beam to a diffraction-limited focal spot[31,32] of 94 nm (FWHM). In the NFH configuration (Fig. 2), the water jet was positioned behind the x-ray focus in the diverging beam. The x-ray holograms were recorded by a sCMOS camera equipped with a fiber-coupled scintillator. It was positioned on-axis in the diverging beam at 9.94 m distance behind the focus [Fig. 2(a)], resulting in a geometrical magnification of 36 and an effective Fresnel number of 1.71×10^{-3}. In the WAXS configuration [Fig. 1(a)], the water jet was placed in the x-ray focus. Two off-axis charge-integrating hybrid pixel detectors (ePix100)[33,34] recorded scattered photons in a scattering vector range of $q \approx 1.4$–2.7 Å^{-1} [Fig. 1(b)]. The detectors were placed in the vertical and horizontal scattering plane with main scattering components $\vec{q}_v$ and $\vec{q}_h$, respectively. The on-axis x-ray camera was used as an intensity monitor in the WAXS configuration.

B. Instrumentation, parameters, and data acquisition

1. XFEL specifications

The linear accelerator of the XFEL accelerated the electrons to an energy of 16.5 GeV into the 175 m-long undulator (magnetic length). A repetition rate of 10 Hz with one pulse per train was used. The undulator delivered photons with an energy of 17.8 KeV. The resulting self-amplified spontaneous emission (SASE) pulses had a pulse width of less than 100 fs (Refs. 25 and 27) and an average pulse energy of 660 μJ.

2. X-ray optics

A stack of 50 beryllium compound refractive lenses (CRLs),[29] aberration corrected by a customized phase plate,[28,30] focused the XFEL pulse to an diffraction limited focal spot of 94 nm (Ref. 31). The CRL stack had a focal length of 475 mm with a numerical aperture of 2.7×10^{-4}. For further details on the experimental parameters, see Refs. 26 and 21 for a detailed characterization of the illumination.

3. X-ray detectors

An Andor Zyla camera (Zyla 5.5, Andor, Abingdon, United Kingdom) was used for the holography measurements. The camera had a LuAg:Ce scintillator (thickness 20 μm), which was coupled to the sCMOS chip with a fiber-optic plate with a pixel size of 6.5 μm. The sample to detector distance was $z_{12} = 9670$ mm. An 8 m long evacuated flight tube reduced air absorption between the sample and detector. For the diffraction measurements, two ePix100 detectors[33,34] were used. The ePix100 is a charge-integrating hybrid pixel detector and consisted of four modules with 384×352 pixels each. The pixel size was 50 μm. The distance between the water jet and the ePix detectors was 250 mm, and the detectors were arranged in an angle of $\sim 12.5^\circ$ toward the x-ray focus.

4. X-ray holography

For the holographic measurements, the water jet was placed in a defocus position of $z_{01} = 271.3$ mm behind the CRL focus, resulting in a geometrical magnification of $M = 36$, an effective pixel size of 177 nm, and an effective Fresnel number of $F = 1.71 \times 10^{-3}$.

5. Laser and laser optics

The pump laser (Nano L 200-10, Litron, Lasers, Rugby, United Kingdom) had a wavelength of 1064 nm, a pulse length of 6 ns, and a maximum pulse energy of 200 mJ. An internal attenuator reduced the pulse energy to 17 mJ. The focusing optics had a numerical aperture of 0.2. The focal spot was expected to exceed the diffraction limited spot size of 1.7 μm (radius $1/e^2$-intensity beam waist) due to aberrations from a through-hole mirror between the focusing lens and water jet. The through-hole mirror was used to get a co-linear alignment of the pump laser and the x-ray beam.

6. μ-fluidic water jet

A μ-fluidic jet (Microliquids GmbH, Göttingen, Germany) with a nozzle diameter of 40 μm was used. The jet nozzle creates a laminar water flow and is connected to a pump (PU-2080, JASCO GmbH, Pfungstadt, Germany) with a flow rate of 1.5 ml min^{-1}. With a jet diameter of 34 μm, measured at the interaction region [cf. Fig. 2(c)], we calculate a mean jet velocity of approximately 28 m s^{-1}. This value agrees well with observations of an optical high-speed camera. For the experiments, de-ionized water at room temperature without additional thermal control of the water reservoir was used.

7. Timing

The timing scheme and equipment are described in great detail in Ref. 26. Here, we will only summarize key parameters. A low jitter delay generator (DG535, Stanford Research Systems, Sunnyvale, CA, USA) controls the pump-probe delay between the XFELs master clock and the Pockels cells of the pump laser. A second delay generator (DG535) was used to keep the delay between the laser's flashlamp and Pockels cell constant at 160 μs for maximum laser output. We determined $\Delta t = 0$ as the delay in which first perturbations are visible in the holography measurements. Note that remaining fluctuations of the IR laser timing, pulse shape, and intensity can lead to a jitter of the breakdown process. For this reason, first perturbations of the pulse-averaged signal $\langle \bar{\phi} \rangle$ are only distinctly visible at $\Delta t = 3$ ns (cf. Figs. 3 and 4).

8. Data acquisition WAXS

To avoid artifacts from a systematic drift in any optical component, we measured the same time delay Δt multiple times in a randomized order. To this end, we acquired ten measurement blocks for each Δt. One block contained $\sim$50 frames. In between these blocks, we acquired $\sim$40 frames of the reference signal without pump-laser output. In total, we acquired 210 of these blocks for delays between -10 and 10 ns in steps of 1 ns and ten blocks for each delay.

III. DATA PROCESSING

Next, we first briefly sketch the processing steps for the phase retrieval of the holographic data, then the processing of the WAXS data. More details are given in Appendixes A and B.

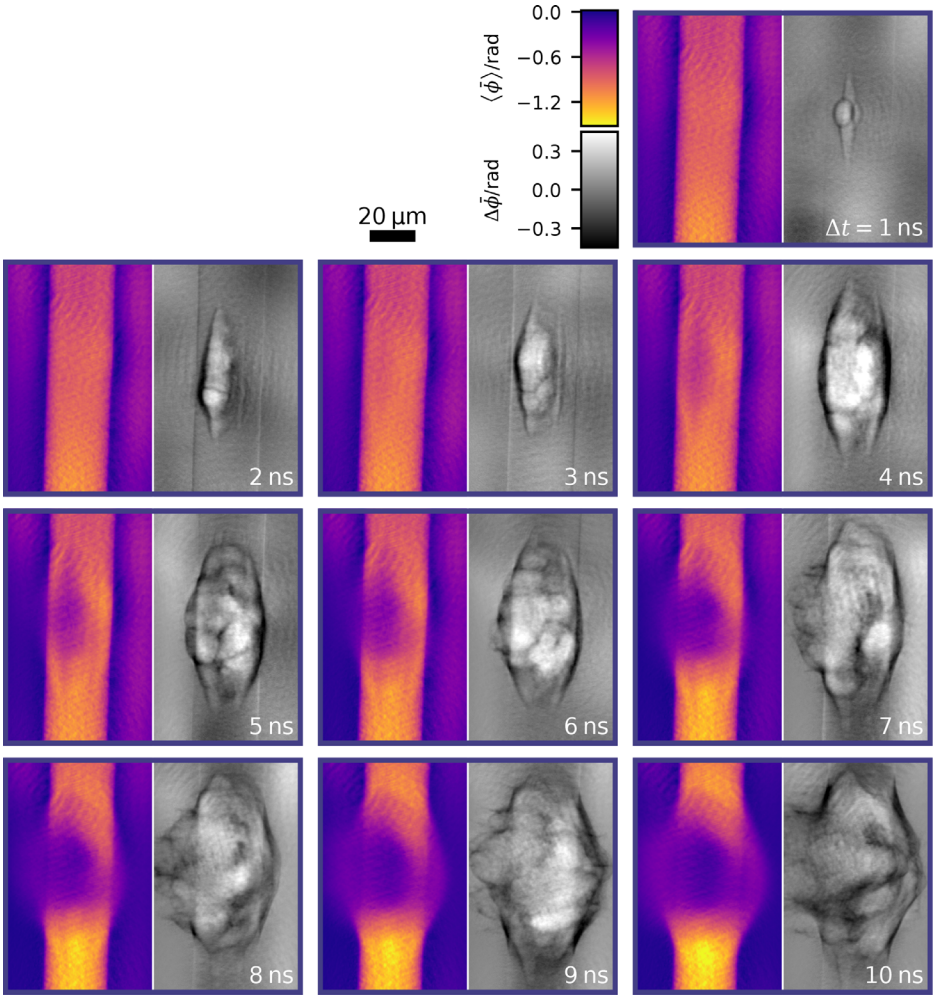

FIG. 3. Time series of phase-shift images from x-ray holography. Pulse-averaged phase shift $\langle\bar{\phi}\rangle$ and an exemplary difference phase shift $\Delta\bar{\phi} = \bar{\phi} - \langle\bar{\phi}\rangle$ (gray scale) for multiple pump-probe delays Δt after laser irradiation. The time series shows the growth of the perturbation in the water jet after dielectric breakdown.

The spontaneous nature of the process of self-amplified spontaneous emission (SASE) does result not only in strong pulse-to-pulse intensity fluctuations but also in fluctuations of the modal composition of the wavefront, impeding a simple empty-beam division for NFH. We have shown in Ref. 21 that SASE pulses are well described by a low-dimensional configuration space, and more importantly, that for a given hologram, an individual empty-beam image can be synthesized by a suitable linear combination of components from a principal component analysis (PCA) of a set of empty-beam images. The phase retrieval, therefore, proceeds in the following two steps: (1) empty-beam correction with the PCA-based approach and (2) phase retrieval with the iterative algorithm alternating projections (AP).[35,36] Examples of an empty-beam corrected single-pulse hologram and the retrieved phase $\bar{\phi}$ are shown in Figs. 2(b) and 2(c). Note that the retrieved phase $\bar{\phi}$ is proportional to the projected electron density of the sample, thus proportional to the projected mass density of water.

The WAXS detection geometry was calibrated with a polycrystalline LaB_6 sample. The intensity measurements were first corrected for a dark current by pedestal subtraction followed by a gain map correction to take gain variations between individual pixels into account (cf. Fig. 9). An x-ray polarization factor was applied to correct for the polarization dependent scattering amplitude (cf. Fig. 11). After azimuthal averaging, a low-pass filter suppressed high frequency noise (cf. Fig. 12). Figure 1(a) shows the corrected diffraction signal of unperturbed water on both detectors. The azimuthal average of the scattered intensity $I(q)$ [Fig. 1(b)] was normalized to the peak intensity.

The pulse-to-pulse SASE fluctuations do not only complicate the empty-beam correction of NFH but also the analysis of the WAXS data, since, in particular, beam pointing fluctuations result in varying background contributions of different optical elements. To mitigate these effects, the WAXS signal was averaged over multiple pulses (see Appendix B).

IV. RESULTS: TIME SERIES OF HOLOGRAPHY AND WAXS DATA

Using the experimental system and data analysis schemes described above, a time-lapse series of (i) phase images and (ii) diffraction patterns was obtained. These data provide quantitative insight into the structural dynamics of the water at molecular scales following

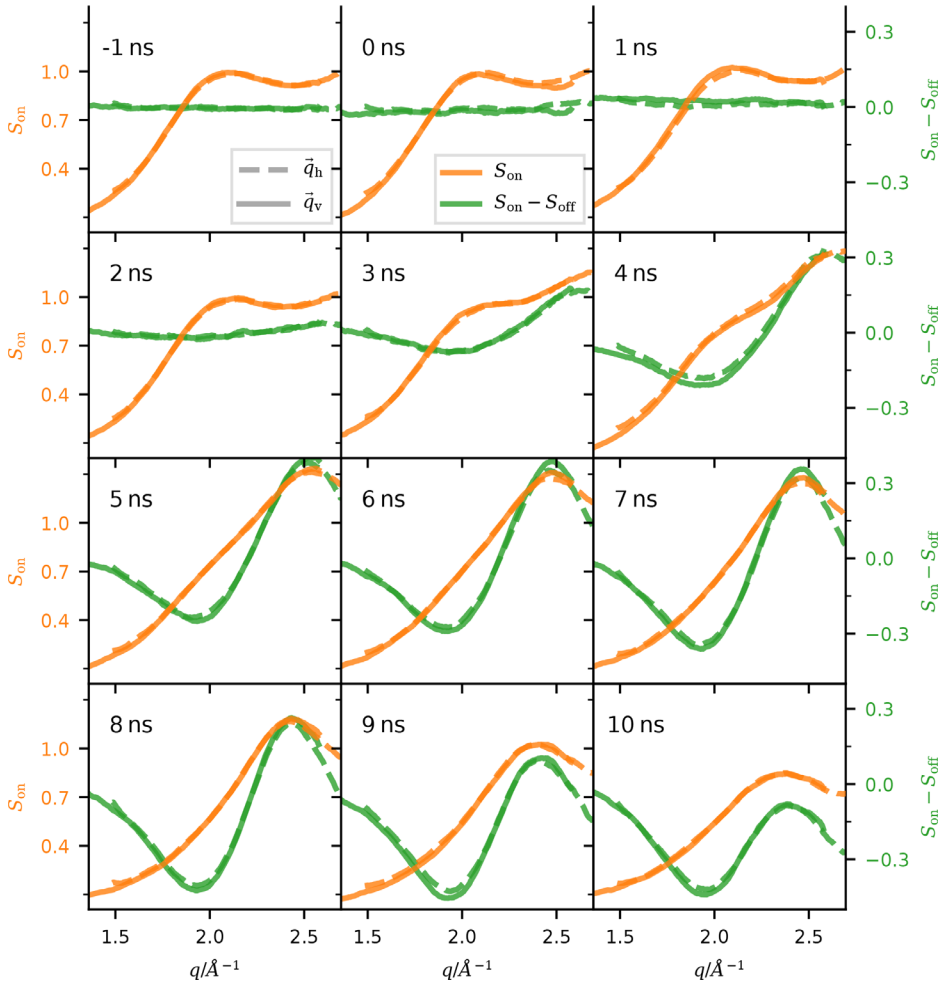

FIG. 4. Time series of the structure factor. Normalized structure factor of perturbed water with pump-laser irradiation (S_{on}, left ordinate) and the difference structure factor between perturbed and unperturbed water $S_{on} - S_{off}$ (right ordinate) for different pump-probe delays Δt. The structure factor is normalized to the maximum value of unperturbed water.

dielectric breakdown, combined with observations of the mesoscale hydrodynamics. The pulse-averaged phase shift[21] $\langle\bar{\phi}\rangle$ (Fig. 3) visualizes the growing perturbation in the water jet after dielectric breakdown in a time series of images, shown here for the case of ∼90 single-pulse reconstructions. Details on individual perturbations without pulse-averaging become apparent when inspecting the phase shift $\bar{\phi}$ retrieved from single-pulse holograms [cf. Fig. 2(b)]. To highlight the variability of the dynamics from an individual perturbation (single-pulse phase shift $\bar{\phi}$), compared to the ensemble dynamics (pulse-averaged phase shift $\langle\bar{\phi}\rangle$), we display the difference phase shift $\Delta\bar{\phi} = \langle\bar{\phi}\rangle - \bar{\phi}$ (Fig. 3), for a sequence of time delays. A small cavitation bubble is visible in $\Delta\bar{\phi}$ at a time delay of 1 ns, followed by a fast expansion at later time delays Δt. Here, we do not only observe the dynamics of the elliptic growth of the perturbation, pushing the outer walls of the water jet apart but also the fine details of water filamentation. A decrease in the magnitude of the average phase shift $\langle\bar{\phi}\rangle$ and, hence, a decrease in the projected mass density start to become visible at $\Delta t = 3$ ns. For later time delays, the projected mass density decreases further to a cavity with ellipsoidal shape.

Figure 4 shows the structure factor $S(q)$ calculated from the diffracted intensity recorded in the WAXS configuration for the same time delays as the NFH measurements. The diffraction signal is dominated by the oxygen atoms in the water molecules with only very weak contributions from the hydrogen atoms. The diffracted intensity $I(q)$ is proportional to the scattering of a single oxygen atom, i.e., the squared form factor $f^2(q)$, and the coherent scattering of the oxygen atoms, described by the structure factor $S(q)$; hence, $I(q) \propto f^2(q)S(q)$ (Ref. 37). The Fourier transform relates the structure factor $S(q)$ to the pair distribution function $g(r)$, describing the structure of the liquid phase in real space.[37] Both scattering directions $\vec{q}_h$ and $\vec{q}_v$ show similar $S(q)$, as expected based on the isotropic distribution of the water molecules, since the laser field is not intense enough to change the orientation of water molecules. $S(q)$ was extracted from the diffracted intensity $I_{on}(q)$ by division of the squared atomic scattering factor $f^2(q)$ for O^{2-} ions.[38] The structure factor was normalized to the maximum value of unperturbed water. At ambient conditions ($\Delta t \leq 0$ ns), the typical doublet structure is observed, albeit not entirely covered by the q-range here. Next, we consider the changes in the measured diffraction intensity $I(q)$, which directly reflects changes in the structure factor $S(q)$ by short range liquid coordination of the water molecules.

Figure 4 shows the structure factor $S(q)$ obtained from our measurements for different time delays Δt. The first slight shift in the

scattering factor becomes apparent at a time delay of 2–3 ns and is clearly visible for time delays $\Delta t \geq 3$ ns. The magnitude of the main diffraction peak at $q \approx 2.0$ Å decreased, whereas a second maximum appears at $q \approx 2.5$ Å, indicating a change in the molecular distances due to rearrangement of the molecules. The latter peak reaches its maximum intensity at about $\Delta t \approx 6$ ns, whereas the initial peak vanishes roughly at the same time delay. For intermediate time delays ($\Delta t \approx 4$ ns), the main peak of $S(q)$ shifts toward higher q, but a shoulder remains at the position of the initial maximum ($q \approx 2.05$ Å), indicating a mixture of water at ambient conditions and water at higher pressures p. This observation agrees well with the holographic data, as the region of lower phase shift magnitude in $\langle\bar{\phi}\rangle$, corresponding to a lower mass density, covers roughly half of the diameter of the water jet for $\Delta t = 4$ ns. For longer time delays ($\Delta t \approx 6$ ns), the contribution of water at ambient conditions quickly vanishes, and the structure factor is dominated by water at higher pressure. Again, this observation is supported by the holographic data, where the initial jet completely vanishes at a time delay between 6 and 7 ns leaving a diffuse cloud of lower mass density. At this delay, the main peak of $S(q)$ starts to shift toward lower values of q. The transition from the typical doublet structure to a single dominating peak can be attributed to a transition from a tetrahedral arrangement of the water molecules toward the molecular structure of a simple liquid, as reported before.[7,15] The vanishing initial peak indicates that the amount of water molecules in its initial state (ambient atmospheric pressure and room temperature) goes down, while a large fraction of water rearranges in response to the quickly rising pressure, as represented by the second peak. The decline in the total scattered intensity for later time delays is most likely caused by an overall reduction of water along the beam path.

Comparing the diffraction signal with the NFH data, first changes are observed in the averaged signal at around $\Delta t = 2$–3 ns. The single-pulse holograms, however, show first changes already from $\Delta t = 1$ ns onward. There are two reasons for this: (1) The seeding rate at small Δt is lower due to a spread of the time point of seeding within the beginning of the 6 ns-long pulse of the pump laser, i.e., not all cavitation bubbles are seeded in the very early beginning of the laser pulse. (2) Variations in the position of the perturbation are on the same length scale as the perturbation itself, since the perturbation is still quite small for small Δt. In the NFH data, the decrease in the magnitude of the averaged phase-shift for $\Delta t \gtrsim 3$ ns implies a reduction in the projected mass density within the region of the perturbation. The decreasing number of water molecules along the beam path should manifest itself in a reduction of the total scattered intensity in the WAXS data; however, this decrease becomes clearly visible only at $\Delta t \gtrsim 8$ ns. This might be explained by the increased scattering intensity of highly pressurized water.

V. RESULTS: WATER STRUCTURE FACTOR AND PRESSURE

In principle, the calculation of the pair distribution function $g(r)$ as the inverse Fourier transform of $S(q)$ would enable us to deduce thermodynamic quantities from the molecular arrangement in real space. This inversion, however, requires $S(q)$ to be measured over a large q-range, impeding the direct inversion of the present data. We, therefore, compared $S(q)$ obtained from the present experiment to published structure factors of water measured for different pressures and temperatures[14,15] to access the pressure dynamics in the water jet after dielectric breakdown. Both studies measured the diffraction of water under well-defined static pressure and temperature conditions in thermal equilibrium using diamond anvil cells and synchrotron radiation. Weck *et al.* obtained data up to a pressure of 4.1 GPa [cf. Fig. 5(a)], whereas Katayama *et al.* measured up to a maximum pressure of 17 GPa. The literature data for the static pressure increase show a shift of the left-most peak (the peak at lowest q) of $S(q)$ toward higher values of q for increasing pressures p, as shown in Fig. 5(a). Using the data of Refs. 14 and 15, the position q_p of this peak can be extracted from $S(q)$ for different pressures p. Specifically, a power-law fit can be used to model the peak position q_p as a function of the pressure p. To this end, $S(q)$ is digitized from the manuscripts using Ref. 39, and the peak position q_p is determined. The following function was then fitted to the data in Fig. 5(b) with pressures $p \geq 0.4$ GPa,

$$\log_{10}(q_p/\text{Å}) = m \cdot \log_{10}(p/\text{GPa}) + b. \quad (1)$$

The least-square fit converged for the values $m = 0.059(2)$ and $b = 0.3665(9)$. Using this fit result, the pressure evolution $p(\Delta t)$ was computed from the peak positions q_p of the structure factor measured in the present work and is finally presented in Fig. 6. The error of the pressure values is dominated by the fit errors. Note as well that the temperature dependence was not taken into account, as it has a negligible influence compared to the pressure (cf. data in Ref. 15). The deduced power-law fit, hence, gives a valid estimation of $q_p(p)$ for values of $p \gtrsim 0.4$ GPa and, thus, enables us to determine pressure values from the present data of the transient pressure increase with sufficient accuracy, despite its limited q-range.

Figure 6(a) shows the structure factor $S(q)$ for different time delays Δt, as in Fig. 4, but now with all curves superimposed. As explained above, $S(q)$ is obtained from the diffracted intensity $I_{on}(q)$

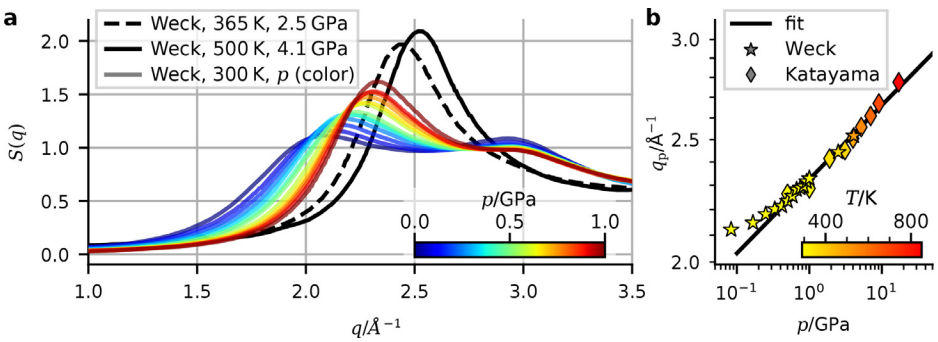

FIG. 5. Structure factor and pressure. (a) Structure factor $S(q)$ of water for different static pressure values p from Ref. 14. (b) Position q_p of the main peak of $S(q)$ for different pressure values p on a double logarithmic scale. The peak position q_p was extracted from data of Weck *et al.*[14] (a) and Katayama *et al.*[15] The power-law fit (black) yields a good approximation for pressure values of $p \gtrsim 0.4$ GPa. Only values with $p \gtrsim 0.4$ GPa were used for fitting.

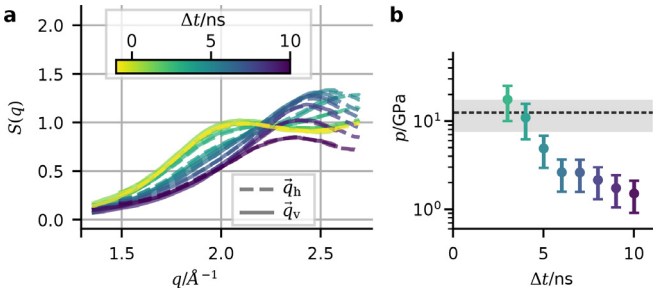

FIG. 6. Dynamics of the structure factor and pressure. (a) Time evolution of the structure factor $S(q)$ of the water jet after dielectric breakdown. (b) Pressure evolution of the water jet after dielectric breakdown. The pressure values were calculated from the position q_p of the main peak of $S(q)$ from (b). The error is dominated by the fit errors (error bars). The pressure values for $\Delta t = 3$ and 4 ns were obtained from an extrapolation of the data to the peak position q_p, as q_p was outside or close to the edge of the measured q-range. The pressure value corresponding to the maximum q value within the measured range is marked (dashed line) and the corresponding error interval (gray area).

(cf. Fig. 13) by division of the squared atomic scattering factor $f^2(q)$ for O^{2-} ions.[38] Furthermore, the structure factor is normalized to the maximum value of unperturbed water. At ambient conditions ($\Delta t \leq 0$ ns), we observe indications for the typical doublet structure, even if not entirely covered by the measured q-range. The transition from the typical doublet structure to a single dominating peak can be attributed to a transition from a tetrahedral arrangement of the water molecules toward the molecular structure of a simple liquid, as reported before.[7,15] Next, we have extracted the peak position q_p from $S(q)$ and used the power-law fit to calculate the pressure p for different time delays Δt. For the time delays 3 and 4 ns, the peak position q_p was outside or close to the boundary of the measured q-range of $S(q)$. We, therefore, manually extrapolated q_p for these two time delays. The resulting pressure evolution [Fig. 6(b)] shows a peak pressure of ~10 GPa, which quickly decays within 7 ns resulting in a pressure of ~1.5 GPa. Note the impressive pressure differences of five orders of magnitude within the thin water jet at early time delays where parts of the jet are still at ambient conditions and parts of the perturbation are at ~10 GPa. This observation is well supported by the NFH data (cf. Fig. 3).

VI. SUMMARY AND CONCLUSION

We have shown that holographic imaging and diffraction (NFH and WAXS) with focused XFEL beams complement each other to obtain information on hydrodynamic and molecular length scales, respectively, with time resolutions, in principle, only limited by the pulse length of the XFEL. We were able to obtain images with quantitative contrast and a field of view on the order of ~100 μm with single-pulse x-ray holography. NFH resolves fine details during the growth of the laser-induced cavity, including shot to shot fluctuations and water filamentation. In the correlated WAXS measurement, we observe a shift of the first peak of the structure factor $S(q)$ of water toward 2.5 $Å^{-1}$ during shock compression. By comparing our data to data from the literature measured at static pressures,[14,15] we report a peak pressure of 10 GPa at $\Delta t = 6$ ns in agreement with our previous study.[22] Importantly, we can attribute the change in the structure factor $S(q)$ after dielectric breakdown to a transition of the structure from a tetrahedral arrangement of water molecules to the molecular structure of a simple liquid.[7,15]

Future extensions of this work will be directed at a wider q-range in order to compute the pair distribution function $g(r)$ using the AGIPD-detector[40] and a higher photon energy. Comparing $g(r)$ to molecular dynamics simulations would then provide a more complete picture of the thermodynamic processes, including pressure as well as temperature traces. Single pulse reconstruction of $g(r)$ of water in a pump-probe scheme could also provide "movies" with molecular time resolution,[41] only limited by the pulse length of the XFEL (less than 100 fs). This is of particular interest for the observation of structural dynamics during the early plasma states of cavitation after dielectric breakdown. Furthermore, comparison of the macroscopic mass density determined by holography with the molecular-scale density obtained from $g(r)$ by diffraction would allow us to detect a possible inhomogeneity in the liquid structure or the presence of domain boundaries. This would be of particular interest for the observation of water in different density configurations and its transitions (LDL to HDL). The future work could compare the imaged mesoscopic density distribution during shock propagation obtained from holographic imaging with hydrodynamic simulations. By probing the molecular structure at different positions along the jet, quantitative density and pressure profiles can be measured not or not easily accessible by other methods.[42–44] To this end, the combined approach of NFH and WAXS could contribute to a comprehensive understanding of cavitation and shock propagation in liquid jets.

To conclude, we have combined two x-ray methods at the XFEL to study the dynamics of water after dielectric breakdown. This allowed us to relate structural information at the molecular scale to quantitative images at mesoscopic scales, where non-equilibrium hydrodynamic phenomena manifest themselves. The combination of techniques, hence, provides the boundary conditions required to interpret the molecular structure in heterogeneous non-equilibrium systems.

ACKNOWLEDGMENTS

We thank C. Schroer, A. Schropp, and F. Seiboth for providing the nanofocusing optics with aberration correction, B. Hartmann and P. Luley for technical help, and the European XFEL for provision of beamtime at the Materials Imaging and Dynamics (MID) instrument. M.V. and T.S. are members of the Max Planck School of Photonics supported by BMBF, Max Planck Society, and Fraunhofer Society. We acknowledge funding by BMBF Projects via Nos. 05K22MG2 and 05K16MGB.

AUTHOR DECLARATIONS

Conflict of Interest

The authors have no conflicts to disclose.

Author Contributions

Malte Vassholz: Conceptualization (equal); Formal analysis (lead); Investigation (lead); Methodology (equal); Software (lead); Validation (lead); Visualization (lead); Writing – original draft (equal); Writing – review & editing (equal). **Joerg Hallmann:** Investigation (supporting); Methodology (supporting). **Chan Kim:** Investigation (supporting); Methodology (supporting). **Alexey V. Zozulya:** Investigation

(supporting); Methodology (supporting). **Wei Lu:** Investigation (supporting); Methodology (supporting). **Roman Shayduk:** Investigation (supporting); Methodology (supporting). **Anders Madsen:** Investigation (supporting); Methodology (supporting); Resources (supporting); Supervision (supporting); Writing – review & editing (supporting). **Tim Salditt:** Conceptualization (equal); Funding acquisition (equal); Investigation (equal); Methodology (equal); Project administration (equal); Supervision (equal); Writing – original draft (equal); Writing – review & editing (equal). **Hannes Paul Hoeppe:** Investigation (equal); Methodology (equal); Software (equal); Validation (equal); Visualization (equal); Writing – review & editing (equal). **Johannes Hagemann:** Formal analysis (supporting); Investigation (supporting); Methodology (equal); Software (equal); Visualization (supporting). **Juan Manuel Rosselló:** Conceptualization (equal); Investigation (equal); Methodology (equal); Writing – review & editing (supporting). **Markus Osterhoff:** Data curation (lead); Formal analysis (supporting); Investigation (equal); Methodology (equal); Software (supporting); Writing – review & editing (supporting). **Robert Mettin:** Conceptualization (supporting); Investigation (supporting); Methodology (supporting); Resources (supporting); Supervision (supporting); Writing – review & editing (supporting). **Johannes Möller:** Investigation (supporting); Methodology (supporting); Writing – review & editing (supporting). **Markus Scholz:** Investigation (supporting); Methodology (supporting). **Ulrike Boesenberg:** Investigation (supporting); Methodology (supporting).

DATA AVAILABILITY

The derived data that support the findings of this study are available from the corresponding author upon reasonable request. Raw data were generated at the European XFEL, MID Instrument, Proposal No. 2544, Ref. 45.

APPENDIX A: DATA PROCESSING—HOLOGRAPHY

An overview over the data processing workflow for NFH is given in Fig. 7(a). The data processing, empty-beam correction, and phase retrieval of the x-ray holograms are described in great detail by Hagemann *et al.*[21] Here, we will only briefly sketch the involved steps.

1. Empty-beam correction

A series of empty-beam images (∼150 images) is acquired directly before and after the measurement of the holograms with the pump laser switched on. The empty-beam correction is based on the components of a principal component analysis (PCA) of the empty-beam series. For each hologram, a reference image is calculated from the first 30 components of the PCA, which is then used for empty-beam division. This approach was first described for data acquired at synchrotrons[46] and was adapted to data from XFELs in Ref. 21.

2. Phase retrieval

The object's phase shift, encoded in the empty-beam corrected x-ray holograms, is retrieved by the iterative phase retrieval algorithm *alternating projections* (AP).[35,36] The algorithm projects the object's guess alternatingly onto a measurement constraint, the intensities of the empty-beam corrected hologram, and a sample constraint, the spatial limitation of the object by a compact support. Two additional sample constraints are used: The range constraint, limiting the phase shift to $\bar{\phi} \in [-10, 0]$ rad, and the homogeneous object constraint with prior knowledge of the δ/β-ratio of water, where δ and β are given by the refracting and absorbing parts of the index of refraction $n = 1 - \delta + i\beta$. The phase retrieval is then divided into two stages: In a first stage, the support for the sample constraint is determined automatically with a maximum number of 500 iterations. In a subsequent second stage, this support is used to calculate the object's phase shift with a maximum of 4000 iterations.

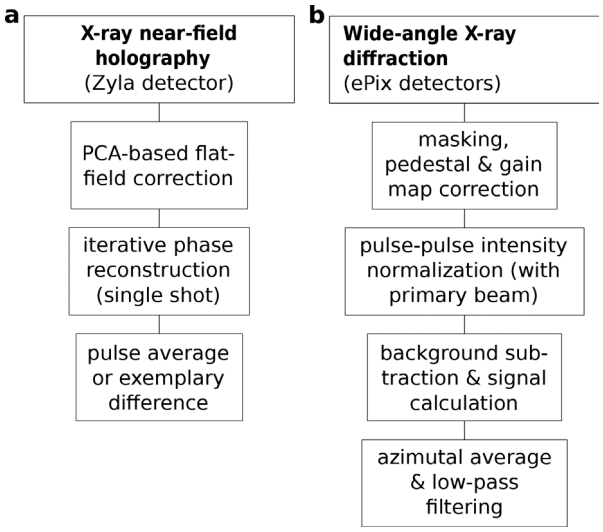

FIG. 7. Data processing steps. (a) X-ray near-field holography (cf. Fig. 2): The PCA-based flat-field correction was performed using a set of empty beam images recorded before and after each run. The phase of the sample is reconstructed numerically by an alternating projections (AP) algorithm for single shot x-ray images. The pulse average phase shift $\langle\bar{\phi}\rangle$ and exemplary difference $\Delta\bar{\phi} = \bar{\phi} - \langle\bar{\phi}\rangle$ are depicted in Fig. 3. (b) X-ray diffraction (cf. Fig. 1): The processing steps are summarized in the schematic and explained in detail in the sections below.

APPENDIX B: DATA PROCESSING—DIFFRACTION DATA

An overview over the data processing workflow for NFH is given in Fig. 7(b).

1. Calibration of the detection geometry

The detection geometry was calibrated with powder diffraction measurements of a polycrystalline LaB_6 sample. Figures 8(a) and 8(b) clearly show the (1 0 0), (1 1 0), and (1 1 1) diffraction rings of the LaB_6 sample on the $\vec{q}_h$ and $\vec{q}_v$ detectors, respectively. We fit three circles with common center position to the diffraction rings on both detectors to determine the detection geometry with respect to the diffraction center. The result is shown in Fig. 8(c). With this diffraction center, the azimuthal average of the detected intensities yields $I(q)$ [Fig. 8(d)]. The calculated positions of the (1 0 0), (1 1 0), and (1 1 1) diffraction peaks for LaB_6 with a lattice constant of 4.16 Å (Ref. 47) are shown.

Note that the images in Figs. 8(a) and 8(b) are not background corrected, only the pedestal was subtracted, such that they give a

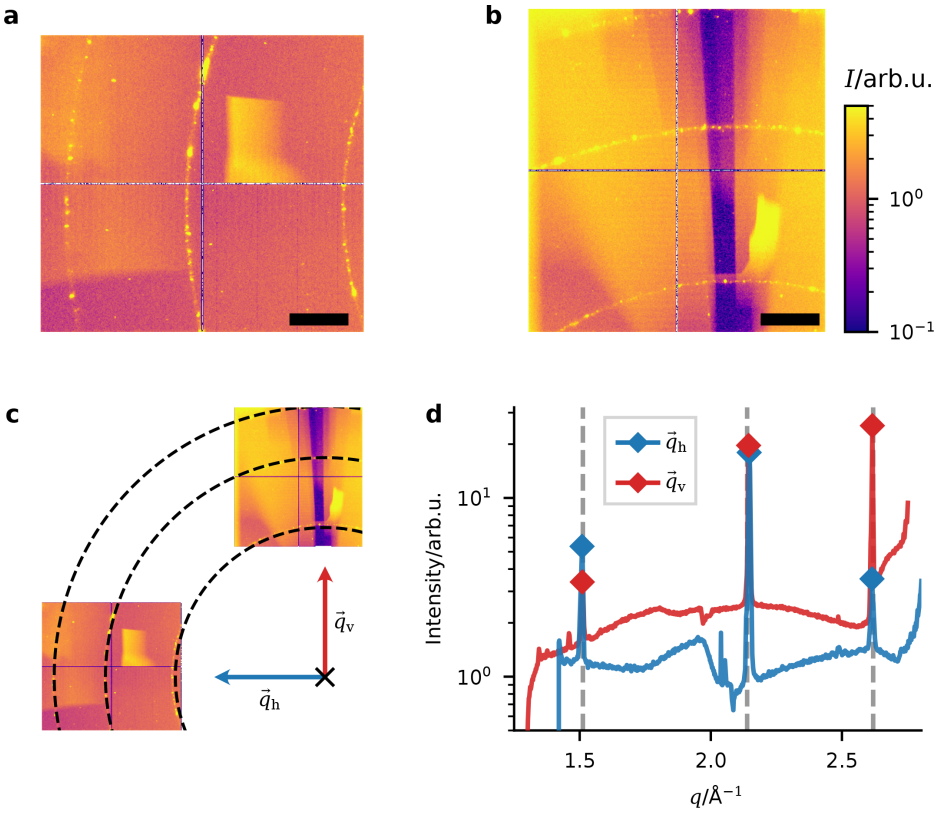

FIG. 8. Calibration of the detection geometry. [(a) and (b)] Detected intensity of the polycrystalline LaB_6 sample after pedestal subtraction for the $\vec{q}_h$ and $\vec{q}_v$ detectors, respectively. The powder diffraction rings of the LaB_6 structure are clearly visible on both detectors. In addition, the images give a good impression of the strong background scattering present in the experiments. (c) Optimized geometry of both detectors. The circles (black, dashed) correspond to the circles fitted to the diffraction rings to calibrate the detection geometry. (d) Diffracted intensity after azimuthal integration of (a) and (b). The vertical lines (gray, dashed) indicate the position of the LaB_6 diffraction peaks from the literature.[47] The diamonds mark the experimentally determined peak positions. Scale bars: 0.2 Å in (a) and (b).

good impression on the background intensity due to scattering at optics and other elements. For example, the vertical blue line in Fig. 8(b) results from a shadowing of the background scattering at the nozzle of the μ-fluidic jet.

2. Detector pedestal and gain-map correction

The pixels of the ePix100 detectors accumulate charge linear to the photon energy incident during the acquisition. Each pixel has to some extent its own readout electronics, leading to different gain factors g_{ij} and pedestals p_{ij} (dark current). The pedestal can easily be corrected by a subtraction of dark images. The correction of different gain factors requires the calculation of a gain map. With monochromatic radiation and low incident flux, the gain map can be calculated by determination of the single photon charge value from pixelwise histograms. Figure 9(a) shows the gain map of the $\vec{q}_h$ detector with a gain variation of ∼15%. The gain-map-corrected intensity measurement shows homogeneous scattering intensity along the diffuse diffraction ring of water, whereas intensity variations are visible in the uncorrected image [cf. Figs. 9(b) and 9(c)].

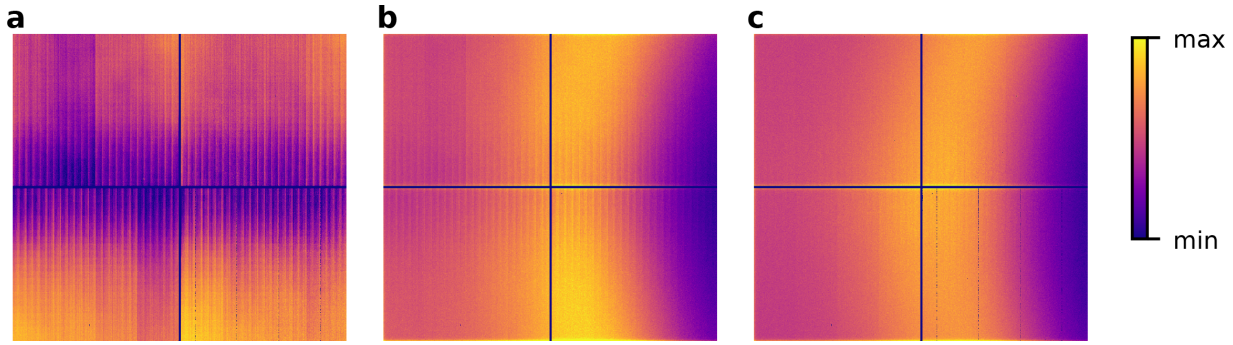

FIG. 9. Gain-map correction of the ePIX100 detectors. The gain map (a) represents the conversion gain per incident 17.5 keV photon for each individual pixel. Strong variations appear between adjacent pixel columns and submodules of the detector chip and in the vertical direction toward the intermodular gap. (b) and (c) Normalized intensity of water diffraction at the $\vec{q}_h$ detector without and with gain correction, respectively. In (a), the color scales linearly with the gain in the range of 250–350 ADU ph^{-1} and in (b) and (c) with the normalized intensity in the range of 0.3–1.6.

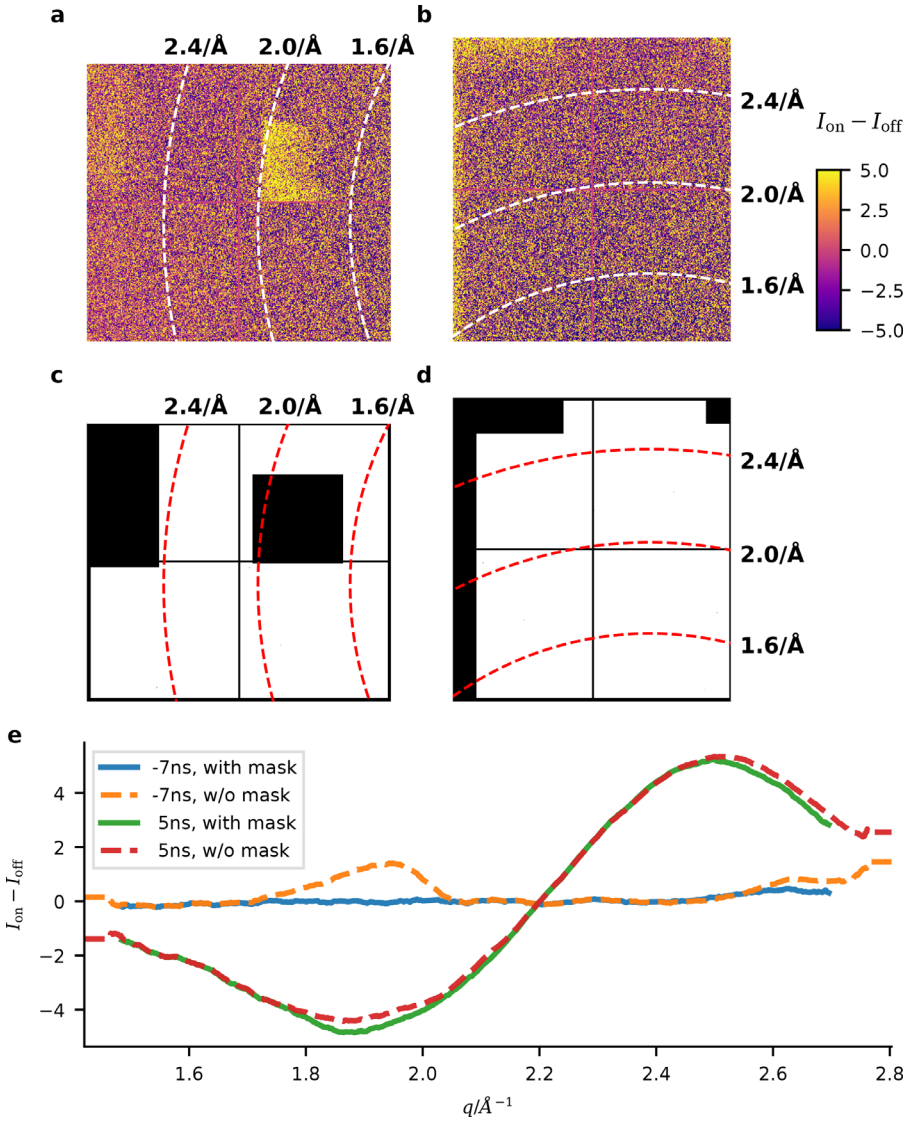

FIG. 10. Masked areas on the diffraction detectors. Areas with strong fluctuations of the background scattering or pedestal are excluded from further analysis. (a) and (b) The difference intensity $I_{on} - I_{off}$ for $\Delta t = -7$ ns (unperturbed water) measured by the $\vec{q}_h$ and $\vec{q}_v$ detectors, respectively. Regions with strong background fluctuations are excluded from further analysis, indicated by the black regions in (c) and (d) for the $\vec{q}_h$ and $\vec{q}_v$ detectors, respectively. (e) Angularly averaged and filtered intensity $I(q)$ of the $\vec{q}_h$ detector for two delays Δt with and without mask (c). The difference intensity in (a)–(c) scales in arbitrary units.

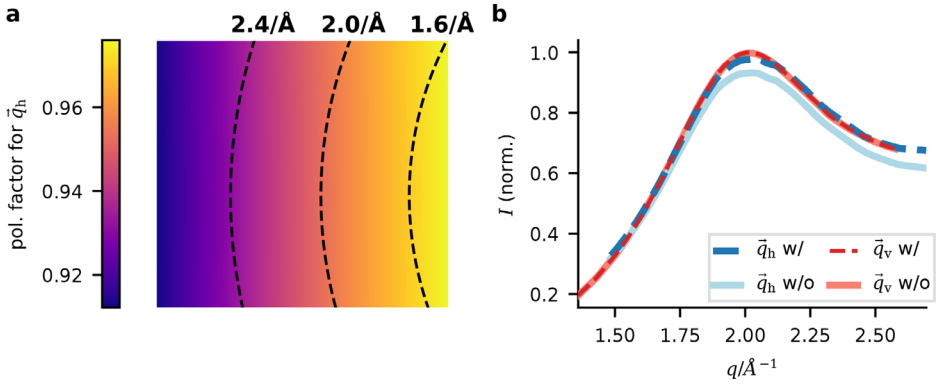

FIG. 11. Polarization correction. (a) Polarization factor for the $\vec{q}_h$ detector with its main scattering contribution parallel to the x-ray polarization. (b) Normalized intensity of water diffraction with and without polarization correction for both detectors. The polarization factor deviates by less than 0.01 from unity on the $\vec{q}_v$ detector with its main scattering contribution perpendicular to the x-ray polarization.

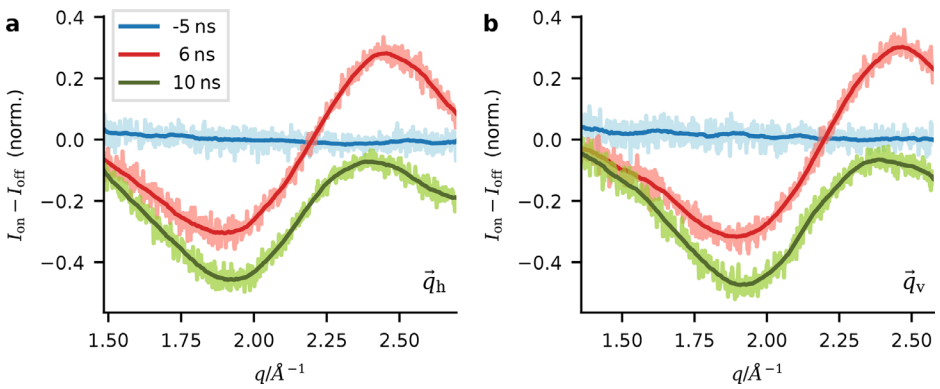

FIG. 12. Signal filtering. Comparison of unfiltered (light colors) and filtered (dark colors) intensity difference $I_{on} - I_{off}$ for three values of Δt. The Savitzky–Golay filter reduces high-frequency noise but leaves the low-frequency variations unchanged. (a) and (b) $\vec{q}_h$ and $\vec{q}_v$ detectors, respectively.

3. Correction of pulse-to-pulse intensity fluctuations

The SASE process leads to strong pulse-to-pulse intensity fluctuations. As the total scattered intensity measured at the ePix100 detectors was not constant with Δt, an external intensity reference was needed. To this end, we corrected each single-pulse diffraction signal by the total intensity measured with the on-axis Zyla camera.

4. Background subtraction and signal calculation

The signal of our interest is the combined signal of the laser-induced perturbation and the unperturbed water jet $\Sigma_{pertub} + \Sigma_{jet}$. The easiest way to obtain this combined signal would be to measure the intensity with pump laser and water jet I_{on} and the background intensity with neither pump laser nor water jet active I_{BG} and

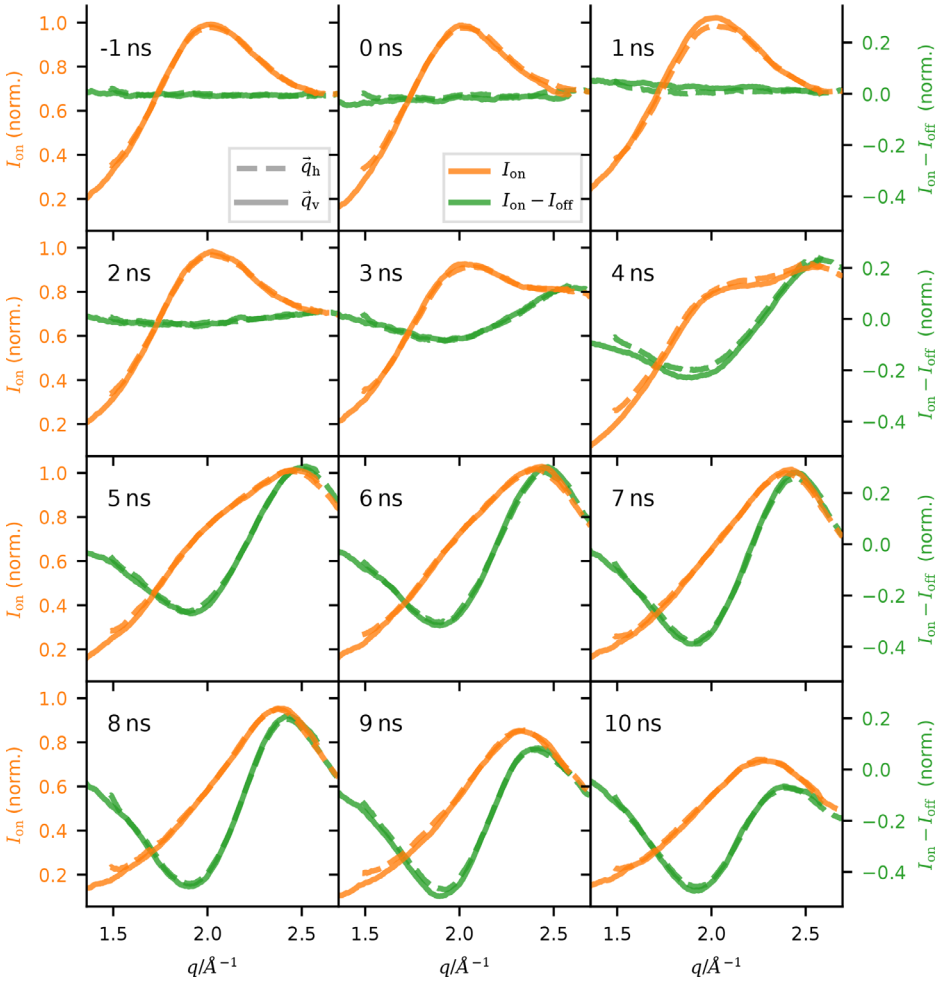

FIG. 13. Time series of the diffracted intensity. Diffracted intensity of the perturbed water jet (I_{on}, left ordinate, orange) and difference in the diffracted intensity with and without laser irradiation ($I_{on} - I_{off}$, right ordinate, green) for different values of the pump-probe delay Δt. Both detectors ($\vec{q}_v$, solid; $\vec{q}_h$, dashed) showed a similar change in the diffracted intensity. Time delays as shown in Figs. 3 and 4.

simply deduce $\Sigma_{\text{pertub}} + \Sigma_{\text{jet}} = I_{\text{on}} - I_{\text{BG}}$. We have to consider, however, that the background intensity is not constant over time due to drifts, so that I_{BG} would have to be measured directly before or after the pump-probe experiment. As we lack this direct measurement of the background, we complemented our overall intensity I_{on} with the intensity obtained in between pump-probe intervals I_{off} after switching off the pump laser, but leaving the water jet running. In an independent measurement, we obtained the intensity with water I_{off} and the background intensity I_{BG} in subsequent measurements. We, thus, end up with $\Sigma_{\text{pertub}} + \Sigma_{\text{jet}} = I_{\text{on}} - I_{\text{off}} + \Sigma_{\text{jet}} = [I_{\text{on}} - I_{\text{off}}]_{t_1} + [I_{\text{off}} - I_{\text{BG}}]_{t_2}$, where t_1 and t_2 indicate the different points in time of acquisition.

5. Detector mask

Some regions on the ePix100 detectors experienced strong pulse-to-pulse fluctuations in the scattering background or pedestal. These areas have been excluded from the analysis (cf. Fig. 10).

6. Polarization correction

The amplitude of the scattered field depends on the polarization of the incoming x-ray wavefield. For horizontally polarized x rays, the full scattering amplitude would only be observed along the vertical axis, i.e., for values of $\vec{q}$ without any contribution in the horizontal direction $\vec{q}_h$. The polarization factor and polarization correction for area detectors are well described in Ref. 48. Let $2\Theta_h$ and $2\Theta_v$ be the scattering angle in the horizontal and vertical planes, respectively. The polarization factor P_h for horizontally polarized x rays is then given by[48]

$$P_h = 1 - \cos^2(2\Theta_v)\,\sin^2(2\Theta_h). \tag{B1}$$

We assume horizontal polarization of the x rays generated within the undulator. Figure 11 shows the polarization factor for the $\vec{q}_h$ detector and the influence on the diffracted intensity $I(q)$.

7. Signal filtering

The $I(q)$ intensity measurements are filtered by a Savitzky–Golay filter [*savgol_filter* of SciPy's signal module (v. 1.5.4)[49] with parameters *polyorder*: 0, *window_length*: 51]. The window length of 51 pixels corresponds to a length in q of ∼0.09 Å. Figure 12 shows a comparison of filtered and unfiltered $I(q)$ for three values of Δt.

For completeness, we also include the evolution of the diffraction intensity I_{on}, before division of the atomic form factor, see Fig. 13.

REFERENCES

[1] A. Nilsson and F. Perakis, "X-ray studies of water," in *Synchrotron Light Sources and Free-Electron Lasers: Accelerator Physics, Instrumentation and Science Applications*, edited by E. J. Jaeschke, S. Khan, J. R. Schneider, and J. B. Hastings (Springer International Publishing, Cham, 2020), pp. 1935–1988.

[2] A. Nilsson and L. G. M. Pettersson, "The structural origin of anomalous properties of liquid water," Nat. Commun. **6**, 8998 (2015).

[3] O. Mishima and H. E. Stanley, "The relationship between liquid, supercooled and glassy water," Nature **396**, 329–335 (1998).

[4] P. G. Debenedetti, "Supercooled and glassy water," J. Phys. **15**, R1669–R1726 (2003).

[5] E. F. Burton, W. F. Oliver, and J. C. McLennan, "The crystal structure of ice at low temperatures," Proc. R. Soc. London, Ser. A **153**, 166–172 (1935).

[6] O. Mishima, L. D. Calvert, and E. Whalley, "'Melting ice' I at 77 K and 10 kbar: A new method of making amorphous solids," Nature **310**, 393–395 (1984).

[7] A. K. Soper and M. A. Ricci, "Structures of high-density and low-density water," Phys. Rev. Lett. **84**, 2881–2884 (2000).

[8] L. B. Skinner, C. J. Benmore, J. C. Neuefeind, and J. B. Parise, "The structure of water around the compressibility minimum," J. Chem. Phys. **141**, 214507 (2014).

[9] J. Russo and H. Tanaka, "Understanding water's anomalies with locally favoured structures," Nat. Commun. **5**, 3556 (2014).

[10] J. A. Sellberg, C. Huang, T. A. McQueen, N. D. Loh, H. Laksmono, D. Schlesinger, R. G. Sierra, D. Nordlund, C. Y. Hampton, D. Starodub, D. P. DePonte, M. Beye, C. Chen, A. V. Martin, A. Barty, K. T. Wikfeldt, T. M. Weiss, C. Caronna, J. Feldkamp, L. B. Skinner, M. M. Seibert, M. Messerschmidt, G. J. Williams, S. Boutet, L. G. M. Pettersson, M. J. Bogan, and A. Nilsson, "Ultrafast X-ray probing of water structure below the homogeneous ice nucleation temperature," Nature **510**, 381–384 (2014).

[11] F. Perakis, K. Amann-Winkel, F. Lehmkühler, M. Sprung, D. Mariedahl, J. A. Sellberg, H. Pathak, A. Späh, F. Cavalca, D. Schlesinger, A. Ricci, A. Jain, B. Massani, F. Aubree, C. J. Benmore, T. Loerting, G. Grübel, L. G. M. Pettersson, and A. Nilsson, "Diffusive dynamics during the high-to-low density transition in amorphous ice," Proc. Natl. Acad. Sci. **114**, 8193–8198 (2017).

[12] K. H. Kim, K. Amann-Winkel, N. Giovambattista, A. Späh, F. Perakis, H. Pathak, M. L. Parada, C. Yang, D. Mariedahl, T. Eklund, T. J. Lane, S. You, S. Jeong, M. Weston, J. H. Lee, I. Eom, M. Kim, J. Park, S. H. Chun, P. H. Poole, and A. Nilsson, "Experimental observation of the liquid-liquid transition in bulk supercooled water under pressure," Science **370**, 978–982 (2020).

[13] K. H. Kim, A. Späh, H. Pathak, C. Yang, S. Bonetti, K. Amann-Winkel, D. Mariedahl, D. Schlesinger, J. A. Sellberg, D. Mendez, G. van der Schot, H. Y. Hwang, J. Clark, O. Shigeki, T. Tadashi, Y. Harada, H. Ogasawara, T. Katayama, A. Nilsson, and F. Perakis, "Anisotropic x-ray scattering of transiently oriented water," Phys. Rev. Lett. **125**, 076002 (2020).

[14] G. Weck, J. Eggert, P. Loubeyre, N. Desbiens, E. Bourasseau, J.-B. Maillet, M. Mezouar, and M. Hanfland, "Phase diagrams and isotopic effects of normal and deuterated water studied via x-ray diffraction up to 4.5 GPa and 500 K," Phys. Rev. B **80**, 180202 (2009).

[15] Y. Katayama, T. Hattori, H. Saitoh, T. Ikeda, K. Aoki, H. Fukui, and K. Funakoshi, "Structure of liquid water under high pressure up to 17 GPa," Phys. Rev. B **81**, 014109 (2010).

[16] T. Strässle, A. M. Saitta, Y. L. Godec, G. Hamel, S. Klotz, J. S. Loveday, and R. J. Nelmes, "Structure of dense liquid water by neutron scattering to 6.5 GPa and 670 K," Phys. Rev. Lett. **96**, 067801 (2006).

[17] A. V. Okhulkov, Y. N. Demianets, and Y. E. Gorbaty, "X-ray scattering in liquid water at pressures of up to 7.7 kbar: Test of a fluctuation model," J. Chem. Phys. **100**, 1578–1588 (1994).

[18] P. C. Myint and J. L. Belof, "Rapid freezing of water under dynamic compression," J. Phys. **30**, 279501 (2018).

[19] M. Millot, F. Coppari, J. R. Rygg, A. Correa Barrios, S. Hamel, D. C. Swift, and J. H. Eggert, "Nanosecond X-ray diffraction of shock-compressed superionic water ice," Nature **569**, 251–255 (2019).

[20] A. Gleason, C. Bolme, E. Galtier, H. Lee, E. Granados, D. Dolan, C. Seagle, T. Ao, S. Ali, A. Lazicki, D. Swift, P. Celliers, and W. Mao, "Compression freezing kinetics of water to ice VII," Phys. Rev. Lett. **119**, 025701 (2017).

[21] J. Hagemann, M. Vassholz, H. Hoeppe, M. Osterhoff, J. M. Rosselló, R. Mettin, F. Seiboth, A. Schropp, J. Möller, J. Hallmann, C. Kim, M. Scholz, U. Boesenberg, R. Schaffer, A. Zozulya, W. Lu, R. Shayduk, A. Madsen, C. G. Schroer, and T. Salditt, "Single-pulse phase-contrast imaging at free-electron lasers in the hard X-ray regime," J. Synchrotron Radiat. **28**, 52 (2021).

[22] M. Vassholz, H. P. Hoeppe, J. Hagemann, J. M. Rosselló, M. Osterhoff, R. Mettin, T. Kurz, A. Schropp, F. Seiboth, C. G. Schroer, M. Scholz, J. Möller, J. Hallmann, U. Boesenberg, C. Kim, A. Zozulya, W. Lu, R. Shayduk, R. Schaffer, A. Madsen, and T. Salditt, "Pump-probe X-ray holographic imaging of laser-induced cavitation bubbles with femtosecond FEL pulses," Nat. Commun. **12**, 3468 (2021).

[23]A. Madsen, J. Hallmann, G. Ansaldi, T. Roth, W. Lu, C. Kim, U. Boesenberg, A. Zozulya, J. Möller, R. Shayduk, M. Scholz, A. Bartmann, A. Schmidt, I. Lobato, K. Sukharnikov, M. Reiser, K. Kazarian, and I. Petrov, "Materials imaging and dynamics (MID) instrument at the European X-ray free-electron laser facility," J. Synchrotron Radiat. **28**, 637 (2021).
[24]T. Tschentscher, C. Bressler, J. Grünert, A. Madsen, A. P. Mancuso, M. Meyer, A. Scherz, H. Sinn, and U. Zastrau, "Photon beam transport and scientific instruments at the European XFEL," Appl. Sci. **7**, 592 (2017).
[25]M. Altarelli, R. Brinkmann, M. Chergui, W. Decking, B. Dobson, S. Düsterer, G. Grübel, W. Graeff, H. Graafsma, J. Hajdu, J. Marangos, J. Pflüger, H. Redlin, D. Riley, I. Robinson, J. Rossbach, A. Schwarz, K. Tiedtke, T. Tschentscher, I. Vartaniants, H. Wabnitz, H. Weise, R. Wichmann, K. Witte, A. Wolf, M. Wulff, and M. Yurkov, "XFEL: The European X-Ray free-electron laser: Technical design report," Report No. DESY 2006-097 (DESY, 2006).
[26]M. Osterhoff, M. Vassholz, H. P. Hoeppe, J. M. Rosselló, R. Mettin, J. Hagemann, J. Möller, J. Hallmann, M. Scholz, R. Schaffer, U. Boesenberg, C. Kim, A. Zozulya, W. Lu, R. Shayduk, A. Madsen, and T. Salditt, "Nanosecond timing and synchronization scheme for holographic pump–probe studies at the MID instrument at European XFEL," J. Synchrotron Radiat. **28**, 987 (2021).
[27]E. Saldin, E. V. Schneidmiller, and M. V. Yurkov, "The physics of free electron lasers," in *Advanced Texts in Physics* (Springer-Verlag, Berlin, Heidelberg, 2000).
[28]F. Seiboth, A. Schropp, M. Scholz, F. Wittwer, C. Rödel, M. Wünsche, T. Ullsperger, S. Nolte, J. Rahomäki, K. Parfeniukas, S. Giakoumidis, U. Vogt, U. Wagner, C. Rau, U. Boesenberg, J. Garrevoet, G. Falkenberg, E. C. Galtier, H. Ja Lee, B. Nagler, and C. G. Schroer, "Perfect X-ray focusing via fitting corrective glasses to aberrated optics," Nat. Commun. **8**, 14623 (2017).
[29]B. Lengeler, C. G. Schroer, M. Kuhlmann, B. Benner, T. F. Günzler, O. Kurapova, F. Zontone, A. Snigirev, and I. Snigireva, "Refractive x-ray lenses," J. Phys. D **38**, A218–A222 (2005).
[30]F. Seiboth, D. Brückner, M. Kahnt, M. Lyubomirskiy, F. Wittwer, D. Dzhigaev, T. Ullsperger, S. Nolte, F. Koch, C. David, J. Garrevoet, G. Falkenberg, and C. G. Schroer, "Hard X-ray wavefront correction via refractive phase plates made by additive and subtractive fabrication techniques," J. Synchrotron Radiat. **27**, 1121–1130 (2020).
[31]C. G. Schroer, B. Lengeler, B. Benner, T. F. Guenzler, M. Kuhlmann, A. S. Simionovici, S. Bohic, M. Drakopoulos, A. A. Snigirev, I. Snigireva, and W. H. Schroeder, "Microbeam production using compound refractive lenses: Beam characterization and applications," in *X-Ray Micro- and Nano-Focusing: Applications and Techniques II*, Vol. 4499 (International Society for Optics and Photonics, 2001), pp. 52–63.
[32]S. Bajt and C. G. Schroer, "Sub-micrometer focusing and high-resolution imaging with refractive lenses and multilayer Laue optics," in *Synchrotron Light Sources and Free-Electron Lasers: Accelerator Physics, Instrumentation and Science Applications*, edited by E. Jaeschke, S. Khan, J. R. Schneider, and J. B. Hastings (Springer International Publishing, Cham, 2019), pp. 1–28.
[33]A. Dragone, P. Caragiulo, B. Markovic, R. Herbst, B. Reese, S. C. Herrmann, P. A. Hart, J. Segal, G. A. Carini, C. J. Kenney, and G. Haller, "ePix: A class of architectures for second generation LCLS cameras," J. Phys. **493**, 012012 (2014).
[34]I. Klačková, G. Blaj, P. Denes, A. Dragone, S. Göde, S. Hauf, F. Januschek, J. Joseph, and M. Kuster, "Characterization of the ePix100a and the FastCCd semiconductor detectors for the European XFEL," J. Instrum. **14**, C01008–C01008 (2019).
[35]D. R. Luke, J. V. Burke, and R. G. Lyon, "Optical wavefront reconstruction: Theory and numerical methods," SIAM Rev. **44**, 169–224 (2002).
[36]J. Hagemann, M. Töpperwien, and T. Salditt, "Phase retrieval for near-field X-ray imaging beyond linearisation or compact support," Appl. Phys. Lett. **113**, 041109 (2018).
[37]J. Als-Nielsen and D. McMorrow, *Elements of Modern X-Ray Physics* (John Wiley & Sons, 2011).
[38]P. J. Brown, A. G. Fox, E. N. Maslen, M. A. O'Keefe, and B. T. M. Willis, "Intensity of diffracted intensities," in *International Tables for Crystallography Volume C: Mathematical, Physical and Chemical Tables*, edited by E. Prince (Springer, Dordrecht, Netherlands, 2004), pp. 554–595.
[39]A. Rohatgi, "Webplotdigitizer: Version 4.4," https://automeris.io/WebPlotDigitizer (2020).
[40]A. Allahgholi, J. Becker, L. Bianco, A. Delfs, R. Dinapoli, P. Goettlicher, H. Graafsma, D. Greiffenberg, H. Hirsemann, S. Jack, R. Klanner, A. Klyuev, H. Krueger, S. Lange, A. Marras, D. Mezza, A. Mozzanica, S. Rah, Q. Xia, B. Schmitt, J. Schwandt, I. Sheviakov, X. Shi, S. Smoljanin, U. Trunk, J. Zhang, and M. Zimmer, "AGIPD, a high dynamic range fast detector for the European XFEL," J. Instrum. **10**, C01023–C01023 (2015).
[41]R. Neutze and K. Moffat, "Time-resolved structural studies at synchrotrons and X-ray free electron lasers: Opportunities and challenges," Curr. Opin. Struct. Biol. **22**, 651–659 (2012).
[42]C. A. Stan, D. Milathianaki, H. Laksmono, R. G. Sierra, T. A. McQueen, M. Messerschmidt, G. J. Williams, J. E. Koglin, T. J. Lane, M. J. Hayes, S. A. H. Guillet, M. Liang, A. L. Aquila, P. R. Willmott, J. S. Robinson, K. L. Gumerlock, S. Botha, K. Nass, I. Schlichting, R. L. Shoeman, H. A. Stone, and S. Boutet, "Liquid explosions induced by x-ray laser pulses," Nat. Phys. **12**, 966–971 (2016).
[43]G. Blaj, M. Liang, A. L. Aquila, P. R. Willmott, J. E. Koglin, R. G. Sierra, J. S. Robinson, S. Boutet, and C. A. Stan, "Generation of high-intensity ultrasound through shock propagation in liquid jets," Phys. Rev. Fluids **4**, 043401 (2019).
[44]D. Ursescu, V. Aleksandrov, D. Matei, I. Dancus, M. D. de Almeida, and C. A. Stan, "Generation of shock trains in free liquid jets with a nanosecond green laser," Phys. Rev. Fluids **5**, 123402 (2020).
[45]J. Hagemann, M. Scholz, and T. Salditt, "Cavitation dynamics studied by time-resolved high-resolution x-ray holography," retrieved from https://in.xfel.eu/metadata/doi/10.22003/XFEL.EU-DATA-002544-00 (2019).
[46]V. Van Nieuwenhove, J. D. Beenhouwer, F. De Carlo, L. Mancini, F. Marone, and J. Sijbers, "Dynamic intensity normalization using Eigen flat fields in X-ray imaging," Opt. Express **23**, 27975–27989 (2015).
[47]I. D. R. Mackinnon, J. A. Alarco, and P. C. Talbot, "Metal Hexaborides with Sc, Ti or Mn," Model. Numer. Simul. Mater. Sci. **3**, 158–169 (2013).
[48]Z. Jiang, "GIXSGUI: A MATLAB toolbox for grazing-incidence X-ray scattering data visualization and reduction, and indexing of buried three-dimensional periodic nanostructured films," J. Appl. Crystallogr. **48**, 917–926 (2015).
[49]P. Virtanen, R. Gommers, T. E. Oliphant, M. Haberland, T. Reddy, D. Cournapeau, E. Burovski, P. Peterson, W. Weckesser, J. Bright, S. J. van der Walt, M. Brett, J. Wilson, K. J. Millman, N. Mayorov, A. R. J. Nelson, E. Jones, R. Kern, E. Larson, C. J. Carey, İ. Polat, Y. Feng, E. W. Moore, J. VanderPlas, D. Laxalde, J. Perktold, R. Cimrman, I. Henriksen, E. A. Quintero, C. R. Harris, A. M. Archibald, A. H. Ribeiro, F. Pedregosa, and P. van Mulbregt, "SciPy 1.0: Fundamental algorithms for scientific computing in Python," Nat. Methods **17**, 261–272 (2020).